

Supporting Information for "Contrasting response of West and East Antarctic ice sheets to Glacial Isostatic Adjustment"

Violaine Coulon¹, Kevin Bulthuis², Pippa L. Whitehouse³, Sainan Sun¹, Konstanze Haubner¹, Lars Zipf¹, Frank Pattyn¹

¹Laboratoire de Glaciologie, Université Libre de Bruxelles, Brussels, Belgium

²Jet Propulsion Laboratory, California Institute of technology, Pasadena, CA, USA

³Department of Geography, Durham University, Durham, UK DH1 3LE

Contents of this file

1. Text S1
 2. Figures S1 to S19
-

Introduction

The following supporting information provides

1. a review of some elements of plate bending theory relevant for GIA models in glaciology and the derivation of the ELRA model for a spatially-varying flexural rigidity (Text S1)
2. additional figures concerning (i) the local sea level calculation (Fig. S1), (ii) WRMS of the predicted uplift rates obtained using specific ice-loading histories (Figs. S2–S3), (iii) the relative sea-level changes observed under RCP 8.5 (Fig. S4), (iv) the behavior of *non-plausible* ensemble members compared to the overall spread of the ensemble (Fig. S5), (v) the behavior of the UNIBED simulation under the four RCP scenarios (Fig. S6), (vi) the behavior of control simulations under various GIA configurations (Figs. S7–S9), (vii) results from the sensitivity analysis of AIS future behavior to GIA processes for different marine basins (Figs. S10–S14), (viii) the ice thickness changes of the UNIBED experiment with a fixed geoid under the four RCP scenarios at various snapshots (Figs. S15–S18), and (iv) uplift rates predicted by the ensemble of 2000 Monte Carlo simulations at 2100 CE (Fig. S19).

Text S1.

Derivation of the ELRA model with a spatially-varying flexural rigidity

In this section, we provide a formal derivation of the ELRA model with a spatially-varying flexural rigidity (equation (7) in the main manuscript). The derivation of the ELRA model can be carried out based on the plate bending theory (Van Wees & Cloetingh, 1994; Ventsel & Krauthammer, 2001). In this context, the equilibrium vertical displacement of the lithosphere in response to an ice loading is described as the equilibrium vertical displacement of a horizontal linear elastic plate subject to a transverse load. In order to represent the viscous asthenosphere underneath the lithosphere, it is also assumed that this plate lies on a viscous substratum. Most of our derivation is based on Ventsel and Krauthammer (2001) but we also refer the reader to Garcia, Sandwell, and Luttrell (2014) for complementary information.

We first present the equation for the equilibrium vertical displacement of an elastic plate with constant thickness (section 1) and its extension to a plate lying on a viscous substratum (section 2). We then present their extensions to an elastic plate with spatially-varying thickness (sections 3 and 4).

1. Plate with constant thickness

Let us consider a thin rectangular plate (which represents the lithosphere in the case of the ELRA model) with constant thickness h (and infinite horizontal dimension). The mechanical properties of the plate are given by its Young's modulus E and its Poisson's ratio ν (both properties are assumed to be constant). The plate is subjected to a transverse

load p (the ice and ocean loadings in the case of the ELRA model), which is a function of the horizontal position $\mathbf{x} = (x, y)$ i.e. $p = p(\mathbf{x})$. Let $w = w(\mathbf{x})$ be the normal displacement of the plate (also called the deflection). For a thin rectangular plate, it is assumed that the shear strains ϵ_{xz} and ϵ_{xy} and the normal strain ϵ_{xx} are negligible, where we denoted the strain tensor by ϵ . In this context and using Hooke's law in linear elasticity (the plate is assumed to behave like a linear elastic material), the components σ_{xy} , σ_{xx} , and σ_{yy} of the stress tensor are given by

$$\sigma_{xx} = \frac{E}{1-\nu^2} (\epsilon_{xx} + \nu \epsilon_{yy}), \quad (1)$$

$$\sigma_{yy} = \frac{E}{1-\nu^2} (\epsilon_{yy} + \nu \epsilon_{xx}), \quad (2)$$

$$\sigma_{xy} = \frac{1}{2} G \epsilon_{xy}, \quad (3)$$

where $G = \frac{E}{2(1+\nu)}$ is the shear modulus. In the context of thin rectangular plates (see equation (2.1) in Ventsel and Krauthammer (2001)), these stress components can be written as

$$\sigma_{xx} = -\frac{Ez}{1-\nu^2} \left(\frac{\partial^2 w}{\partial x^2} + \nu \frac{\partial^2 w}{\partial y^2} \right), \quad (4)$$

$$\sigma_{yy} = -\frac{Ez}{1-\nu^2} \left(\frac{\partial^2 w}{\partial y^2} + \nu \frac{\partial^2 w}{\partial x^2} \right), \quad (5)$$

$$\sigma_{xy} = -\frac{Ez}{1+\nu} \frac{\partial^2 w}{\partial x \partial y}, \quad (6)$$

where the vertical coordinate z is measured from the middle surface of the plate.

The resulting twisting (or torsion) moments M_{xx} and M_{yy} and bending moment M_{xy} (equal to M_{yx}) are given by

$$M_{xx} = \int_{-h/2}^{h/2} \sigma_{xx} z dz = -D \left(\frac{\partial^2 w}{\partial x^2} + \nu \frac{\partial^2 w}{\partial y^2} \right), \quad (7)$$

$$M_{yy} = \int_{-h/2}^{h/2} \sigma_{yy} z dz = -D \left(\frac{\partial^2 w}{\partial y^2} + \nu \frac{\partial^2 w}{\partial x^2} \right), \quad (8)$$

$$M_{xy} = \int_{-h/2}^{h/2} \sigma_{xy} z dz = -D(1 - \nu) \frac{\partial^2 w}{\partial x \partial y}, \quad (9)$$

where

$$D = \frac{Eh^3}{12(1 - \nu^2)} \quad (10)$$

is the *flexural rigidity of the plate*.

Writing the equilibrium of forces and moments for the plate (see equations (2.19)–(2.21) in Ventsel and Krauthammer (2001)), it can be shown that the twisting and bending moments satisfy the following differential equation (see equation (2.23) in Ventsel and Krauthammer (2001)):

$$\frac{\partial^2 M_{xx}}{\partial x^2} + 2 \frac{\partial^2 M_{xy}}{\partial x \partial y} + \frac{\partial^2 M_{yy}}{\partial y^2} = -p. \quad (11)$$

Substituting equations (7)–(9) into equation (11) gives the following partial differential equation for the deflection w :

$$\frac{\partial^2}{\partial x^2} \left(-D \left(\frac{\partial^2 w}{\partial x^2} + \nu \frac{\partial^2 w}{\partial y^2} \right) \right) + 2 \frac{\partial^2}{\partial x \partial y} \left(-D(1 - \nu) \frac{\partial^2 w}{\partial x \partial y} \right) + \frac{\partial^2}{\partial y^2} \left(-D \left(\frac{\partial^2 w}{\partial y^2} + \nu \frac{\partial^2 w}{\partial x^2} \right) \right) = -p, \quad (12)$$

or as D is assumed to be constant and ν is constant

$$-D \left(\frac{\partial^4 w}{\partial x^4} + 2\nu \frac{\partial^4 w}{\partial x^2 \partial y^2} + \frac{\partial^4 w}{\partial y^4} \right) - 2D(1 - \nu) \frac{\partial^4 w}{\partial x^2 \partial y^2} = -p, \quad (13)$$

that is,

$$D \left(\frac{\partial^4 w}{\partial x^4} + 2 \frac{\partial^4 w}{\partial x^2 \partial y^2} + \frac{\partial^4 w}{\partial y^4} \right) \equiv D \nabla_x^4 w = p. \quad (14)$$

2. Plate with constant thickness on a viscous substratum

We consider now that the plate (lithosphere) in section 1 lies on a viscous substratum (the asthenosphere) with density ρ_a . In this case, we must account for the buoyancy force (which depends on the vertical displacement w) that the lithosphere experiences in the underlying viscous substratum. The buoyancy force acts to reduce the exerted load p by an amount $\rho_a g w$ (hydrostatic pressure of the asthenosphere). Then, equation (14) writes in the presence of a viscous substratum as

$$D\nabla_{\mathbf{x}}^4 w + \rho_a g w = p. \quad (15)$$

This equation is simply the equation for the deflection of the lithosphere in the ELRA model (equation (1) in the main manuscript).

For a general applied load p , a solution to the linear partial differential equation (15) can be established using a superposition principle. Indeed, the Green's function for the linear differential operator $D\nabla_{\mathbf{x}}^4 + \rho_a g$ writes as (Hertz, 1884; Nadai, 1963)

$$G(\mathbf{x}) = -\frac{L^2}{2\pi D} \text{kei}\left(\frac{\|\mathbf{x}\|}{L}\right), \quad (16)$$

where kei denotes the zeroth-order Kelvin function and $L = \sqrt[4]{D/(\rho_a g)}$ is the so-called radius of relative stiffness (or flexural length scale), which determines the non-locality of the plate displacement. Using the superposition principle, the solution to the linear partial differential equation (15) can be expressed as

$$w(\mathbf{x}) = G(\mathbf{x}) * p(\mathbf{x}) = \int_{\mathbb{R}^2} -\frac{L^2}{2\pi D} \text{kei}\left(\frac{\|\mathbf{x} - \mathbf{x}'\|}{L}\right) p(\mathbf{x}') d\mathbf{x}', \quad (17)$$

where $*$ denotes the convolution operator. The use of this Green's function provides an efficient way to solve for the deflection of the lithosphere due to ice loading in numerical ice-sheet models (see for instance (Pattyn, 2017; Pollard & DeConto, 2012)).

3. Plate with spatially-varying thickness

Let us consider in this section a thin rectangular plate having a spatially-varying thickness $h = h(\mathbf{x})$ (and infinite horizontal dimension). As in section 1, the plate is assumed to behave as a linear elastic material with constant Young's modulus E and Poisson's ratio ν . The plate is subjected to a transverse load $p = p(\mathbf{x})$ that induces a deflection $w = w(\mathbf{x})$ of the plate. Following section 3.8 in Ventsel and Krauthammer (2001), we assume that the thickness varies gradually and there is no abrupt variation in thickness so that the expressions for the bending and twisting moments introduced earlier for plates of constant thickness (see equations (7)–(9)) also apply with sufficient accuracy to the case of a thin rectangular plate having a spatially-varying thickness. Please note that in this case, the flexural rigidity D is therefore spatially varying i.e.

$$D = D(\mathbf{x}) = \frac{Eh(\mathbf{x})^3}{12(1 - \nu^2)}. \quad (18)$$

Substituting equations (7)–(9) with the spatially-varying flexural rigidity $D(\mathbf{x})$ into equation (11) gives the following partial differential equation for the deflection w :

$$\begin{aligned} \frac{\partial^2}{\partial x^2} \left(-D(\mathbf{x}) \left(\frac{\partial^2 w}{\partial x^2} + \nu \frac{\partial^2 w}{\partial y^2} \right) \right) + 2 \frac{\partial^2}{\partial x \partial y} \left(-D(\mathbf{x})(1 - \nu) \frac{\partial^2 w}{\partial x \partial y} \right) \\ + \frac{\partial^2}{\partial y^2} \left(-D(\mathbf{x}) \left(\frac{\partial^2 w}{\partial y^2} + \nu \frac{\partial^2 w}{\partial x^2} \right) \right) = -p, \end{aligned} \quad (19)$$

where we have highlighted the dependence of D on the horizontal position \mathbf{x} . Please note that although this equation is identical to equation (12), it cannot be reduced to the simple equation (14) due to the fact that the spatially-varying flexural rigidity $D(\mathbf{x})$ cannot be simply drawn out of the derivatives. Arranging the different terms in equation (19) (using Leibniz rule for derivation), one obtains the following equation for the deflection of a plate having a spatially-varying flexural rigidity (see equation (3.83) in Ventsel and

Krauthammer (2001)):

$$\begin{aligned} D\nabla_x^4 w + 2\frac{\partial D}{\partial x}\frac{\partial}{\partial x}(\nabla_x^2 w) + 2\frac{\partial D}{\partial y}\frac{\partial}{\partial y}(\nabla_x^2 w) + \nabla_x^2 D(\nabla_x^2 w) \\ -(1-\nu)\left(\frac{\partial^2 D}{\partial x^2}\frac{\partial^2 w}{\partial y^2} - 2\frac{\partial^2 D}{\partial x \partial y}\frac{\partial^2 w}{\partial x \partial y} + \frac{\partial^2 D}{\partial y^2}\frac{\partial^2 w}{\partial x^2}\right) = p. \end{aligned} \quad (20)$$

Please note that in the latter equation, the Poisson's ratio of the plate appears explicitly in the equation. Also, this equation involves both the gradient of the flexural rigidity (through its first derivatives) and the curvature of the flexural rigidity (through its second derivatives). All the terms in equation (20) involving derivatives of the flexural rigidity are nil when the plate has a constant thickness and therefore a constant flexural rigidity.

4. Plate with spatially-varying thickness on a viscous substratum

We consider now that the plate (lithosphere) in section 3 lies on a viscous substratum (the asthenosphere) with density ρ_a . Similarly to section 2, we must account for the buoyancy force (which depends on the vertical displacement w) that the lithosphere experiences in the underlying viscous substratum. Then, equation (20) writes in the presence of a viscous substratum as

$$\begin{aligned} D\nabla_x^4 w + 2\frac{\partial D}{\partial x}\frac{\partial}{\partial x}(\nabla_x^2 w) + 2\frac{\partial D}{\partial y}\frac{\partial}{\partial y}(\nabla_x^2 w) + \nabla_x^2 D(\nabla_x^2 w) \\ -(1-\nu)\left(\frac{\partial^2 D}{\partial x^2}\frac{\partial^2 w}{\partial y^2} - 2\frac{\partial^2 D}{\partial x \partial y}\frac{\partial^2 w}{\partial x \partial y} + \frac{\partial^2 D}{\partial y^2}\frac{\partial^2 w}{\partial x^2}\right) + \rho_a g w = p. \end{aligned} \quad (21)$$

This equation is simply the equation for the equilibrium deflection of the lithosphere in the ELRA model with spatially-varying flexural rigidity (equation (7) in the main manuscript)

Please note that contrary to section 2 and to our knowledge, there exists no Green's function that allows to write the solution to equation (21) as a superposition principle. In this case, equation (21) is solved using numerical methods such as finite-difference methods or finite-element methods.

References

- Argus, D. F., Peltier, W. R., Drummond, R., & Moore, A. W. (2014). The Antarctica component of postglacial rebound model ICE-6G_C (VM5a) based on GPS positioning, exposure age dating of ice thicknesses, and relative sea level histories. *Geophysical Journal International*, 198, 537–563. doi: <https://doi.org/10.1093/gji/ggu140>
- Garcia, E. S., Sandwell, D. T., & Luttrell, K. M. (2014). An iterative spectral solution method for thin elastic plate flexure with variable rigidity. *Geophysical Journal International*, 200(2), 1012-1028. doi: <https://doi.org/10.1093/gji/ggu449>
- Goelzer, H., Coulon, V., Pattyn, F., de Boer, B., & van de Wal, R. (2020). Brief communication: On calculating the sea-level contribution in marine ice-sheet models. *The Cryosphere*, 14(3), 833–840. doi: 10.5194/tc-14-833-2020
- Hertz, H. (1884). Ueber das gleichgewicht schwimmender elastischer platten. *Annalen der Physik*, 258(7), 449-455. doi: <https://doi.org/10.1002/andp.18842580711>
- Le Meur, E., & Huybrechts, P. (1996). A comparison of different ways of dealing with isostasy: examples from modelling the Antarctic ice sheet during the last glacial cycle. *Annals of Glaciology*, 23, 309–317. doi: <https://doi.org/10.1017/epic.12717.d001>
- Nadai, A. (1963). Theory of flow and fracture of solids. In (Vol. 2). New York, NY: McGraw-Hill Book Company.
- Pattyn, F. (2017). Sea-level response to melting of Antarctic ice shelves on multi-centennial timescales with the fast Elementary Thermomechanical Ice Sheet model (f.ETISh v1.0). *Cryosphere*, 11, 1–28. doi: <https://doi.org/10.5194/tc-11-1-2017>
- Pollard, D., & DeConto, R. M. (2012). Description of a hybrid ice sheet-shelf model , and application to Antarctica. *Geoscientific Model Development*, 5, 1273–1295. doi:

<https://doi.org/10.5194/gmd-5-1273-2012>

Van Wees, J. D., & Cloetingh, S. (1994). A finite-difference technique to incorporate spatial variations in rigidity and planar faults into 3-d models for lithospheric flexure. *Geophysical Journal International*, 117(1), 179-195. doi: <https://doi.org/10.1111/j.1365-246X.1994.tb03311.x>

Ventsel, E., & Krauthammer, T. (2001). *Thin plates and shells* (1st ed.). Boca Raton: CRC Press. doi: <https://doi.org/10.1201/9780203908723>

Whitehouse, P. L., Bentley, M. J., & Le Brocq, A. M. (2012). A deglacial model for antarctica: geological constraints and glaciological modelling as a basis for a new model of antarctic glacial isostatic adjustment. *Quaternary Science Reviews*, 32, 1 - 24. doi: <https://doi.org/10.1016/j.quascirev.2011.11.016>

Whitehouse, P. L., Bentley, M. J., Milne, G. A., King, M. A., & Thomas, I. D. (2012). A new glacial isostatic adjustment model for antarctica: calibrated and tested using observations of relative sea-level change and present-day uplift rates. *Geophysical Journal International*, 190(3), 1464-1482. doi: <https://doi.org/10.1111/j.1365-246X.2012.05557.x>

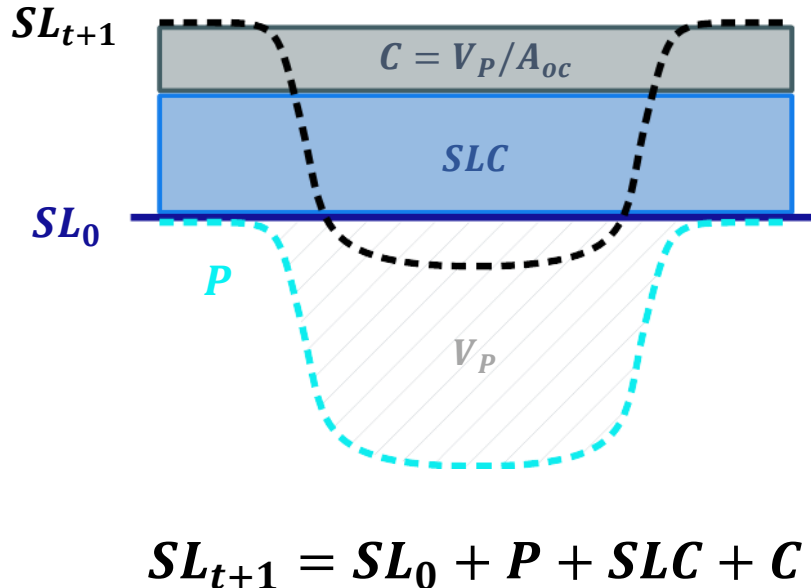


Figure S1. Schematic 2D representation of local sea-level change calculations. Local sea level at time $t + 1$, SL_{t+1} (black dashed line), is calculated as the sum of the initial sea surface SL_0 (dark blue solid line), the geoid perturbation P due to mass changes m_G (light blue dashed line), the barystatic sea-level contribution arising from Antarctic ice mass changes (SLC , calculated as in Goelzer et al. (2020)) and a mass conservation term C , which is a spatial constant that must be added to the solution in order to conserve oceanic mass. C is calculated by redistributing the volume change across ocean areas due to P (V_P) over the ocean area A_{oc} .

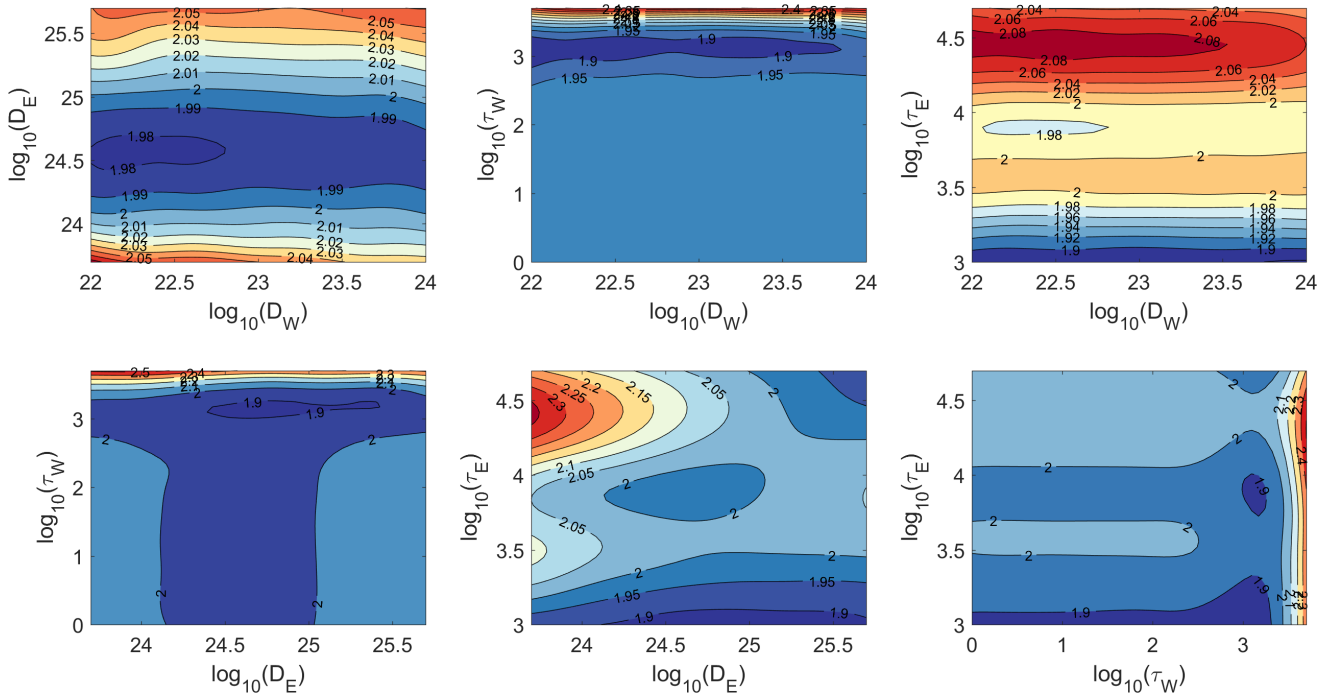


Figure S2. Weighted Root-Mean Square (WRMS, see equation B1) of the predicted uplift rates obtained using W12 ice-loading history (Whitehouse, Bentley, & Le Brocq, 2012) relative to present-day uplift rates (Whitehouse, Bentley, Milne, et al., 2012). As a comparison, predicted uplift rates obtained using uniform ELRA parameters ($\tau=8000$ yr (Argus et al., 2014) and $D = 10^{25}$ N m (Le Meur & Huybrechts, 1996)) give a WRMS of 2.97 mm/yr. Units for D_E are N m and units for τ_E are years.

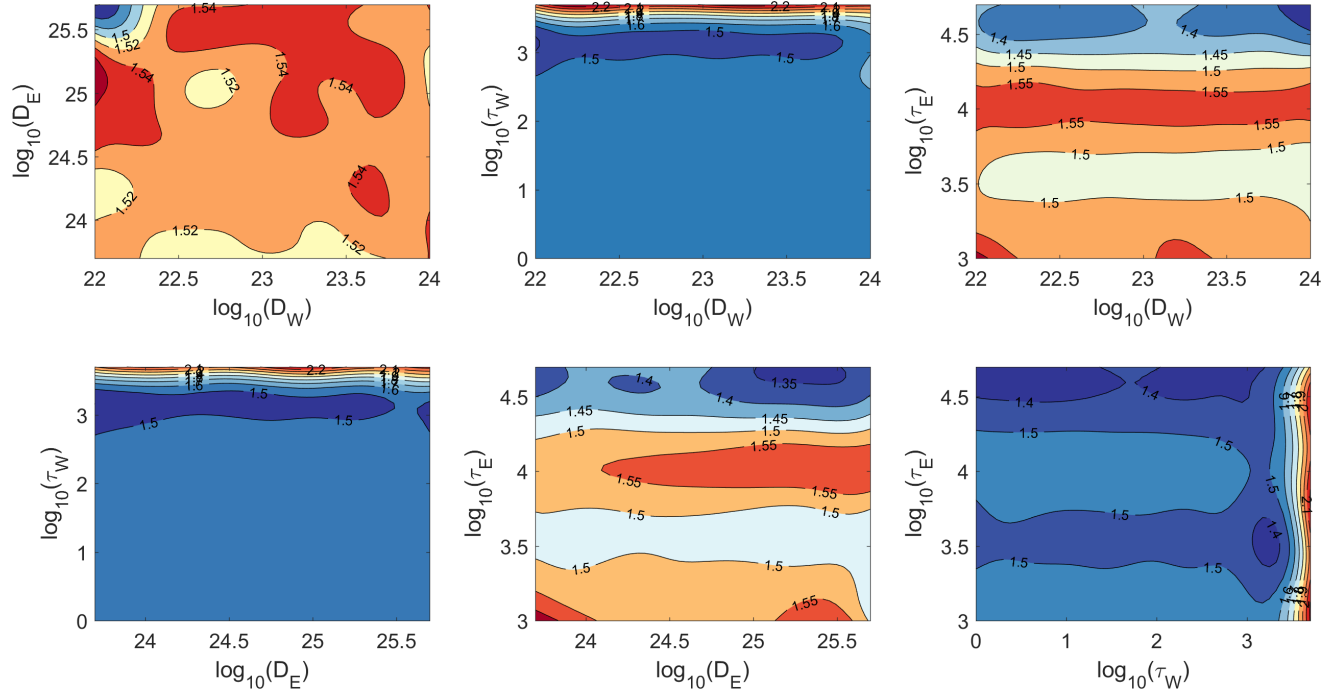


Figure S3. Weighted Root-Mean Square (WRMS, see equation B1) of the predicted uplift rates obtained using ICE-6G ice-loading history (Argus et al., 2014) relative to present-day uplift rates (Whitehouse, Bentley, Milne, et al., 2012). As a comparison, predicted uplift rates obtained using uniform ELRA parameters ($\tau=4000$ yr (Argus et al., 2014) and $D = 10^{25}$ N m (Le Meur & Huybrechts, 1996)) give a WRMS of 2.12 mm/yr. Units for D_E are N m and units for τ_E are years.

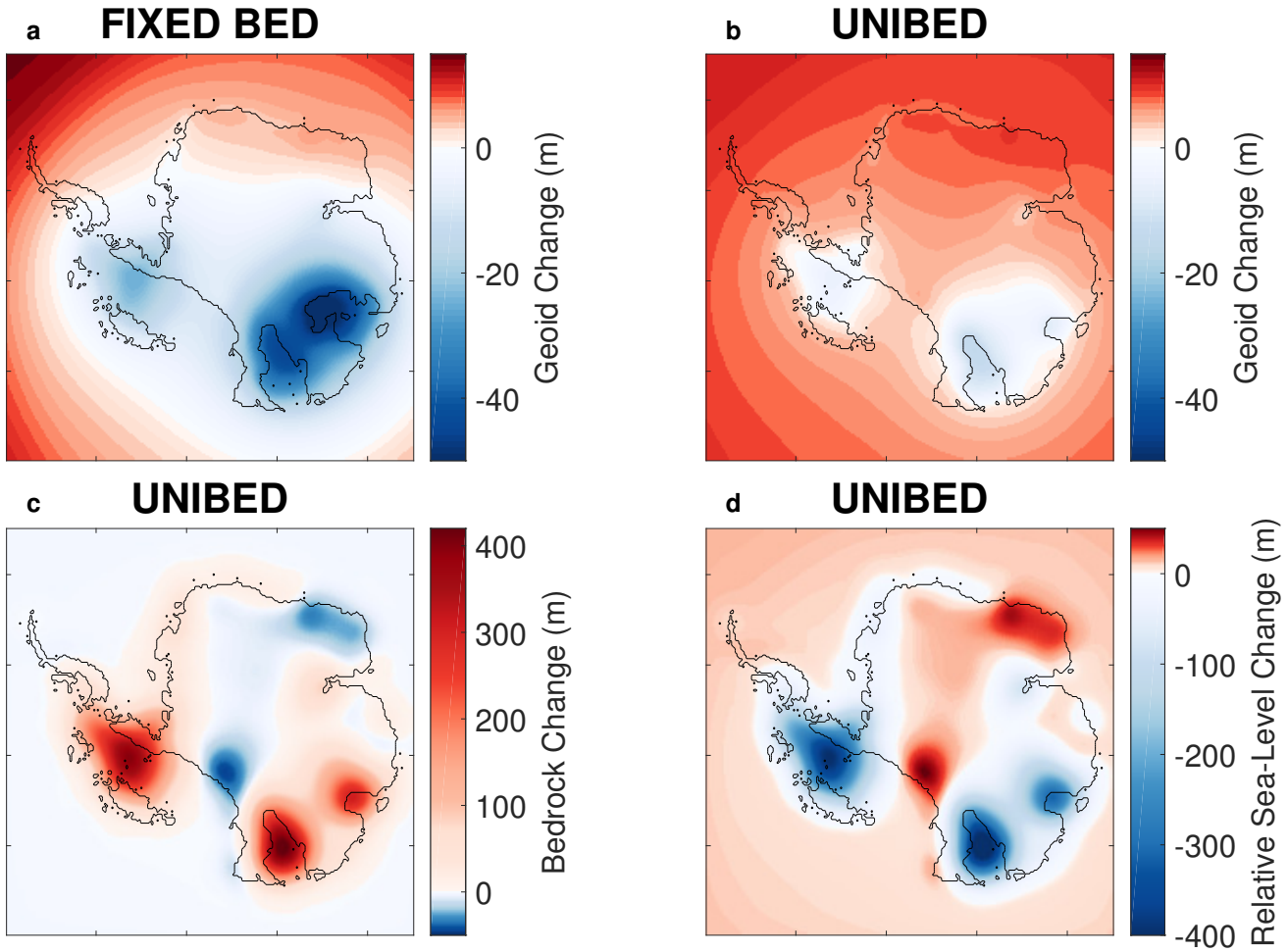


Figure S4. Relative sea-level changes at 7000 CE under RCP 8.5 for a simulation with a fixed bedrock (a), and a simulation where bedrock adjustment is considered (b–d). Relative sea-level changes due to geoid change are displayed in (a–b). Bedrock changes are displayed in (c). Note that relative sea-level changes due to bedrock changes are the opposite of (c). Total relative sea-level changes – i.e. the combination of geoid and bedrock changes – are displayed in (a) for the simulation with a fixed bedrock (FIXED BED) and in (d) for a simulation where bedrock adjustment is considered (UNIBED, with uniform ELRA parameters taken from Le Meur and Huybrechts (1996)). When bedrock adjustment is considered, geoid changes (b) have a smaller contribution to relative sea-level change (d) than bedrock changes (c). In addition, note that the gravitational effect of changes in the distribution of mantle material associated with solid earth deformation counteracts geoid changes due to ice and ocean mass changes, leading to geoid changes of smaller amplitude in (b) than in (a).

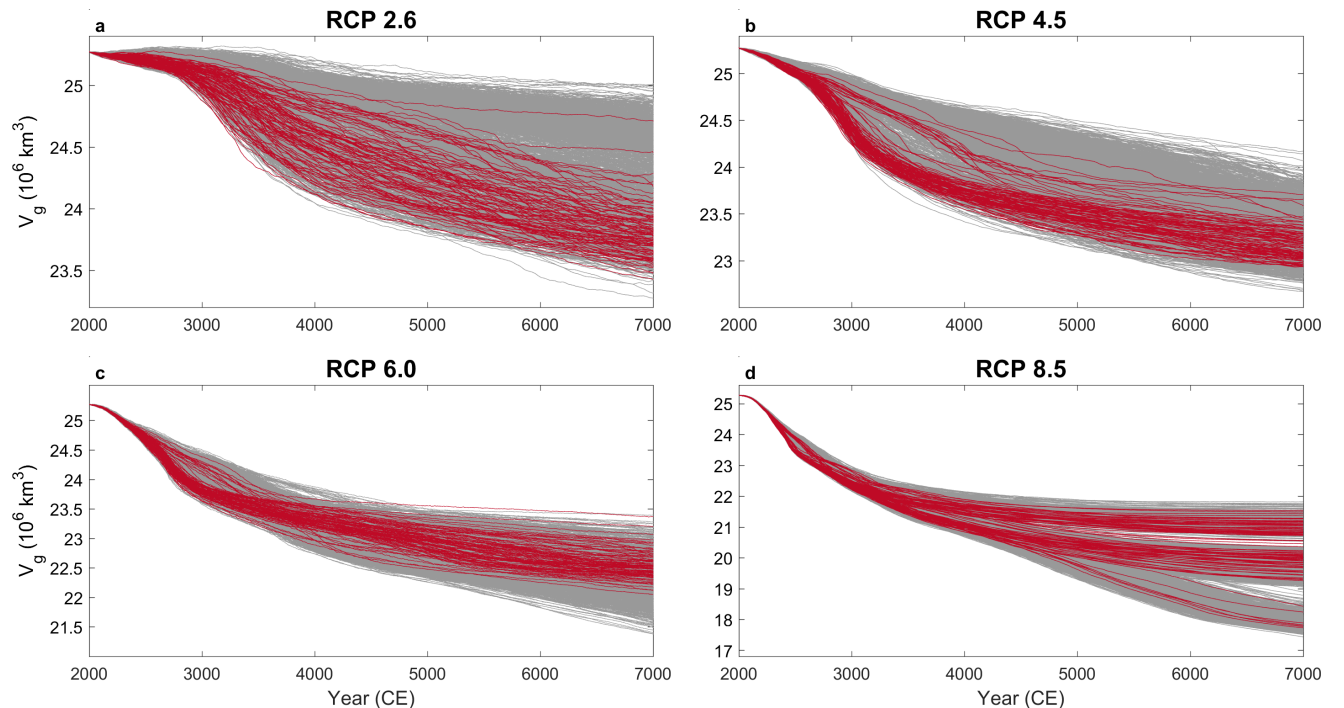


Figure S5. Projections of Antarctic grounded-ice volume (V_g) under RCP 2.6 (a), 4.5 (b), 6.0 (c), and 8.5 (d). Grey lines represent time series of Antarctic grounded-ice volume for the 1900 *plausible* Monte Carlo ensemble members while red line represent those of the 100 *non-plausible* Monte Carlo ensemble members (i.e. either $D_W > D_E$ or $\tau_W > \tau_E$).

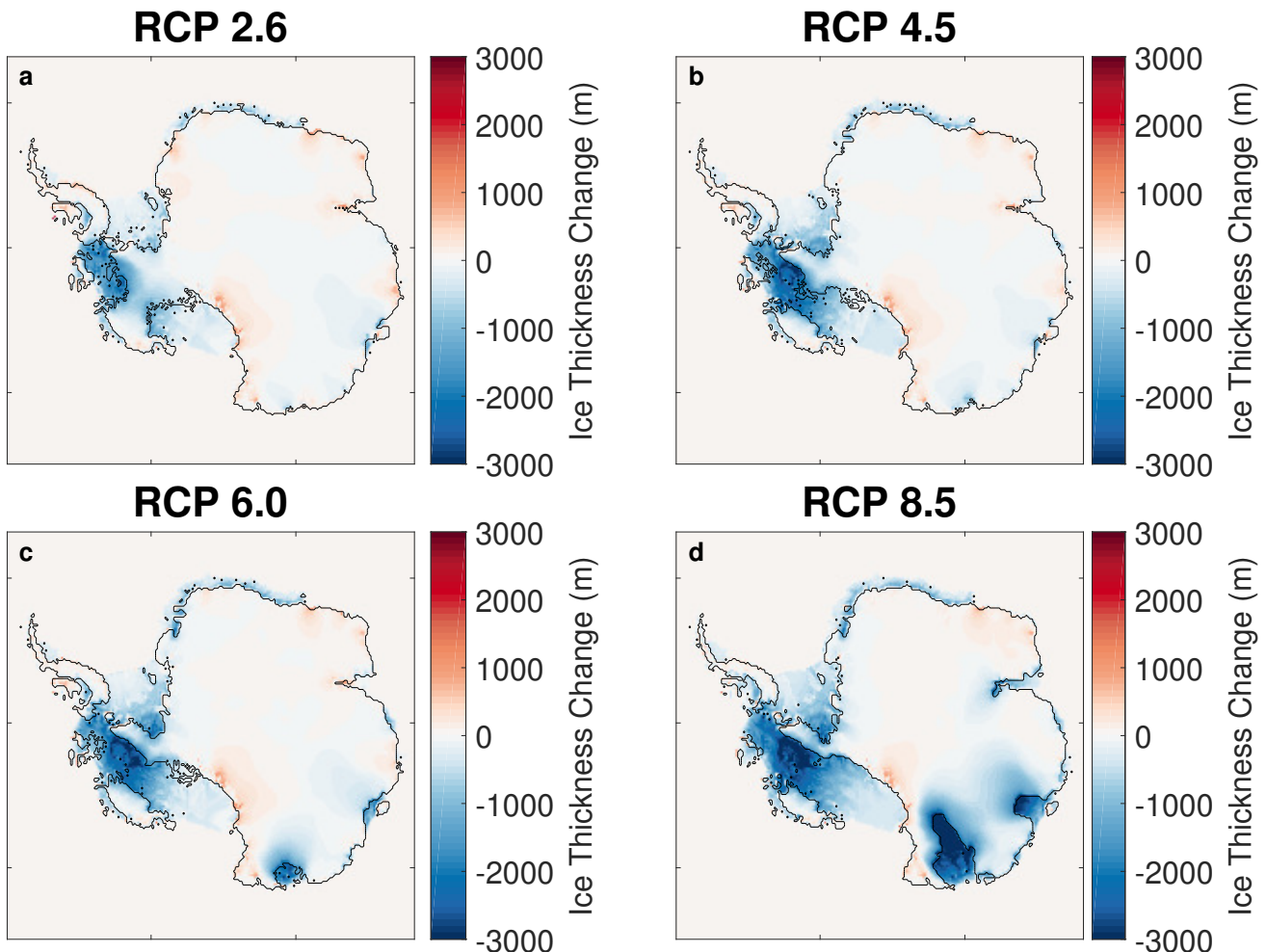


Figure S6. Change in Antarctic ice thickness at 7000 CE for the UNIBED simulations (with uniform ELRA parameters taken from Le Meur & Huybrechts, 1996) under (a) RCP 2.6, (b) RCP 4.5, (c) RCP 6.0, and (d) RCP 8.5.

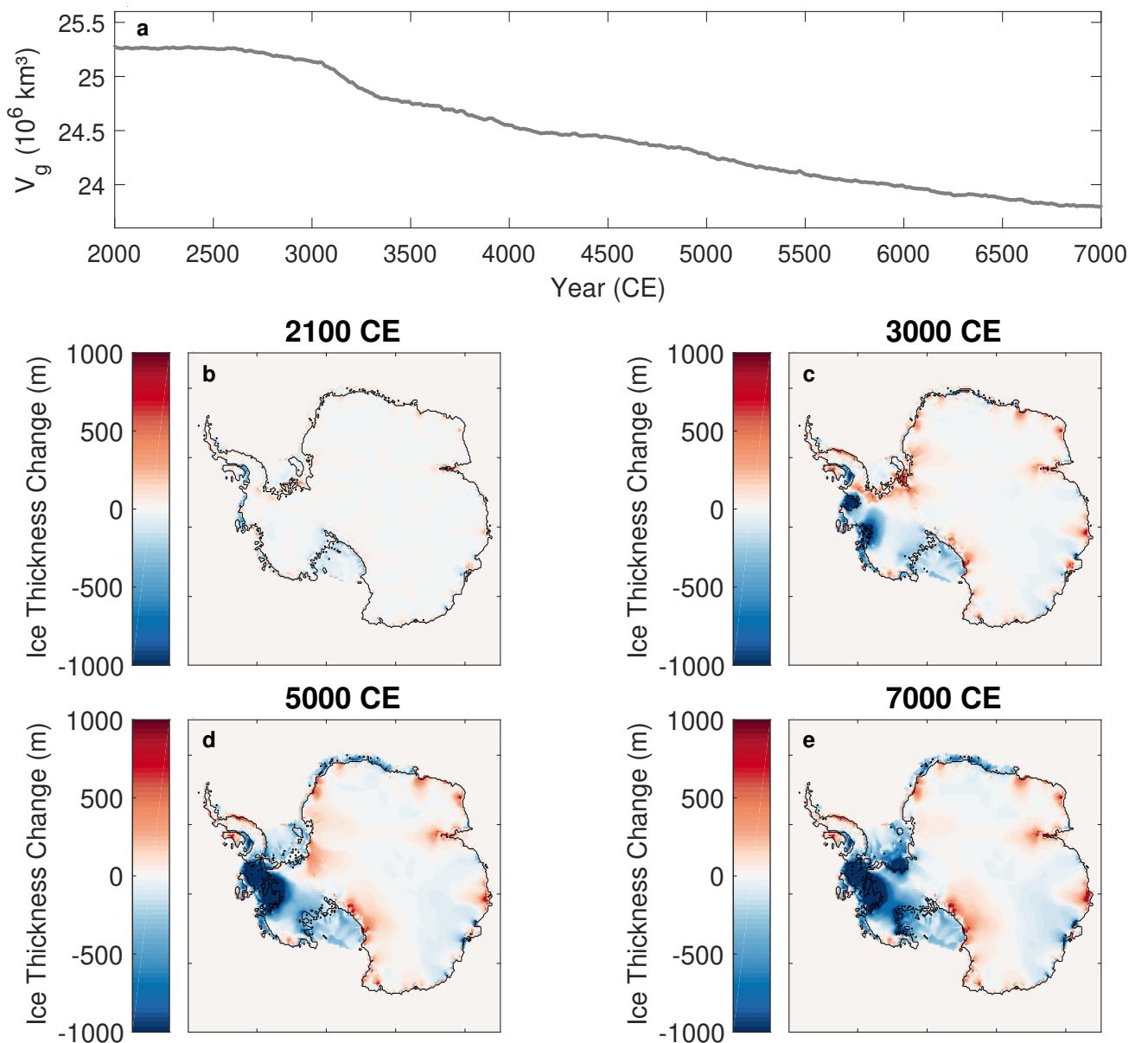


Figure S7. Evolution of Antarctic grounded-ice volume V_g (a) and ice thickness change at 2100 CE (b), 3000 CE (c), 5000 CE (d), and 7000 CE (e) for a control NOGIA (bedrock and geoid are fixed) simulation under constant present-day climate (no climatic perturbation).

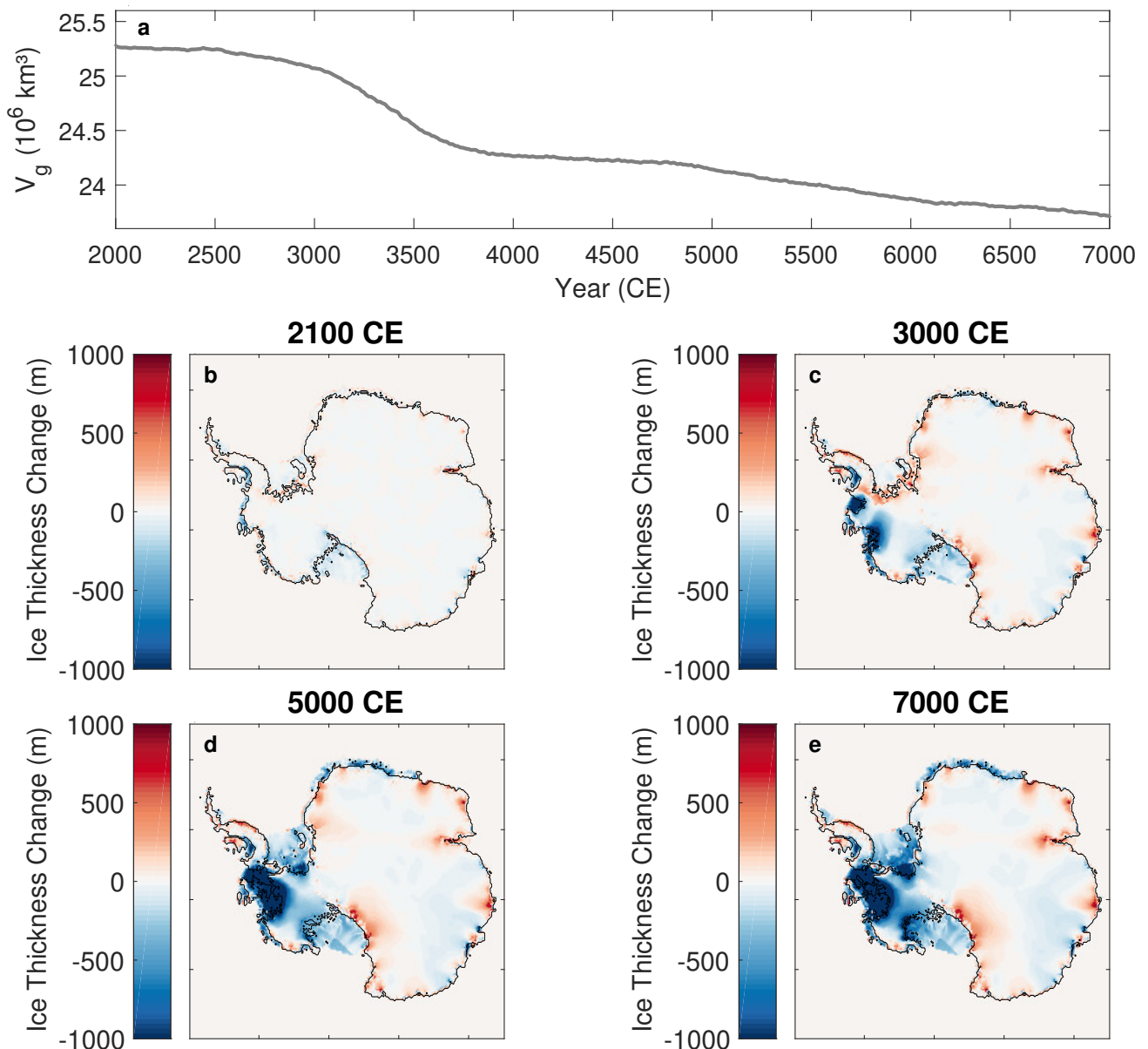


Figure S8. Evolution of Antarctic grounded-ice volume V_g (a) and ice thickness change at 2100 CE (b), 3000 CE (c), 5000 CE (d), and 7000 CE (e) for a control simulation under constant present-day climate (no climatic perturbation) for which uniform ELRA parameters (UNIBED) from Le Meur and Huybrechts (1996) are considered.

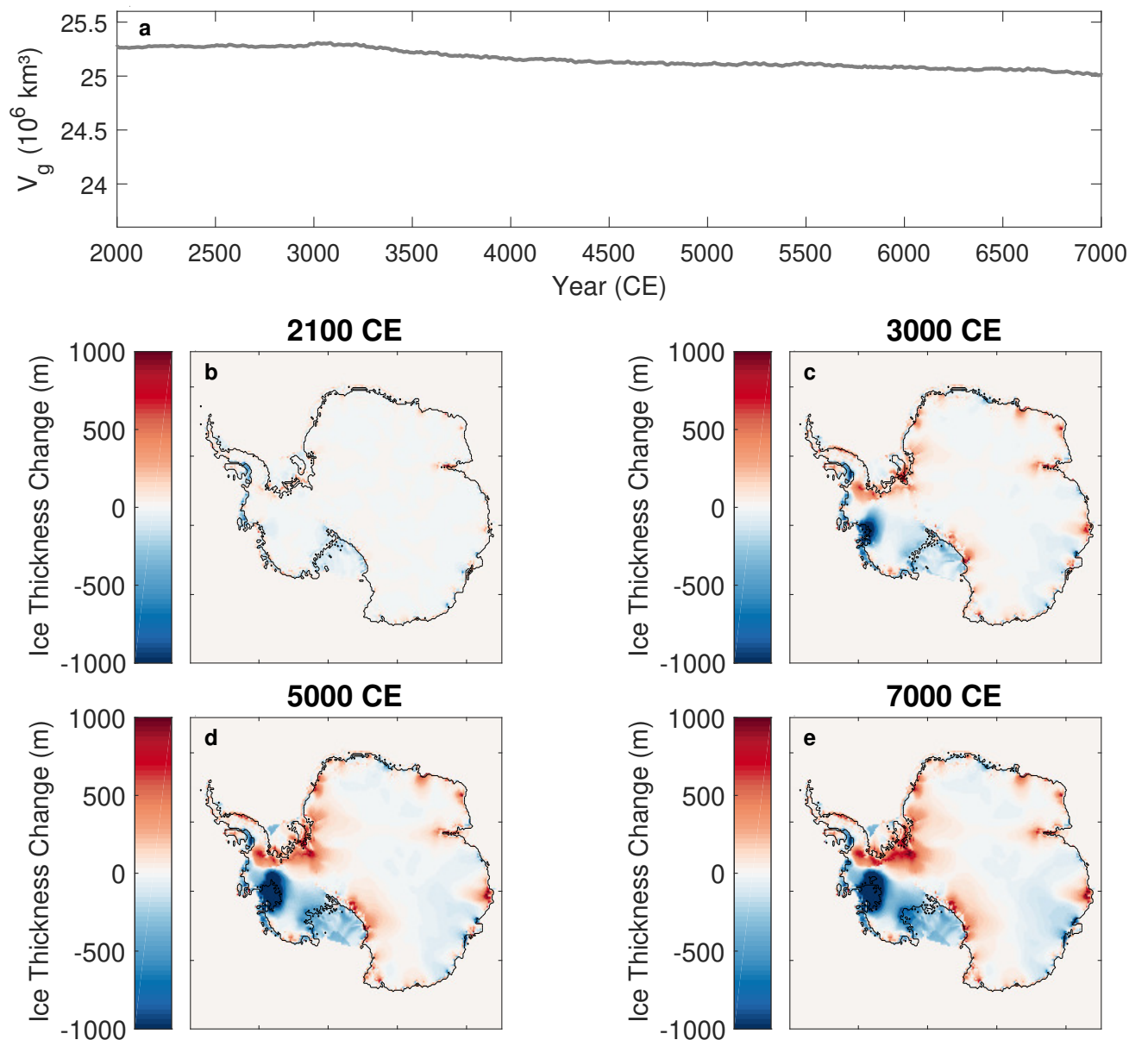


Figure S9. Evolution of Antarctic grounded-ice volume V_g (a) and ice thickness change at 2100 CE (b), 3000 CE (c), 5000 CE (d), and 7000 CE (e) for a control simulation under constant present-day climate (no climatic perturbation) for which median values of the ELRA parameters are considered.

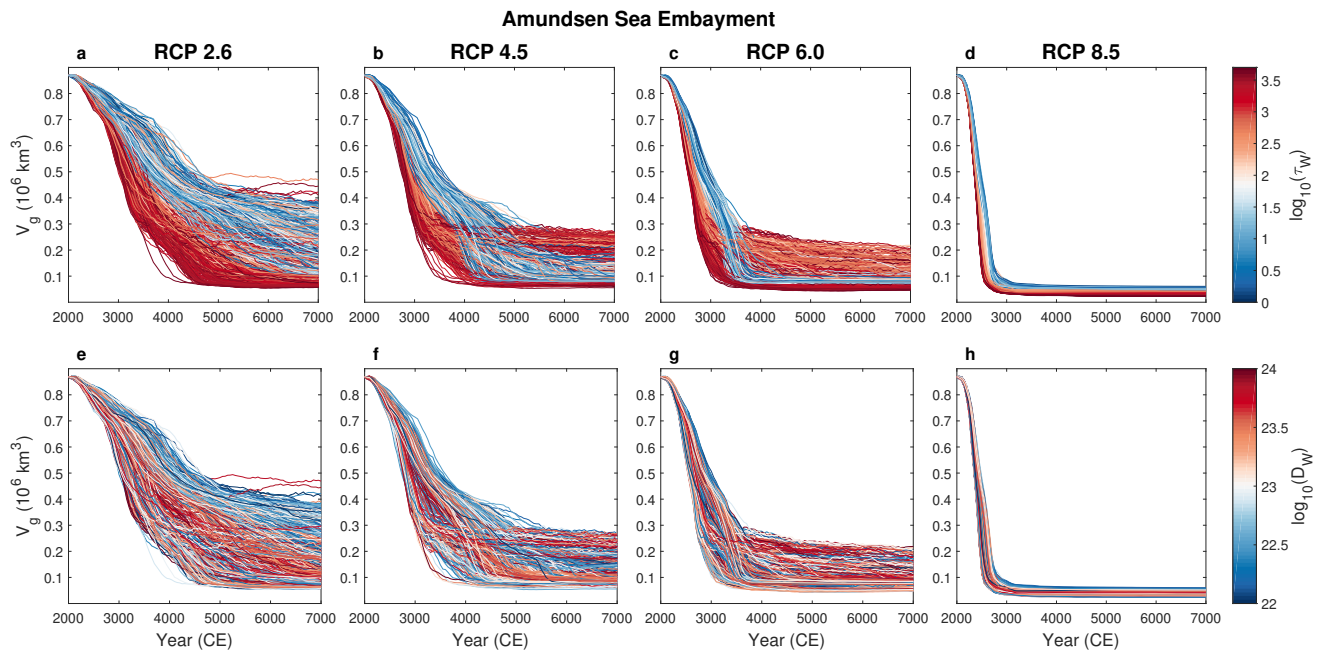


Figure S10. Evolution of Amundsen Sea Embayment grounded-ice volume under RCP 2.6 (a, e), 4.5 (b, f), 6.0 (c, g), and 8.5 (e, h) for 2000 Monte Carlo samples from the parameter space. Time-series of the ensemble are color-coded by values of (a–d) $\log_{10}(\tau_W)$ and (e–h) $\log_{10}(D_W)$. Units for D_W are N m and units for τ_W are years.

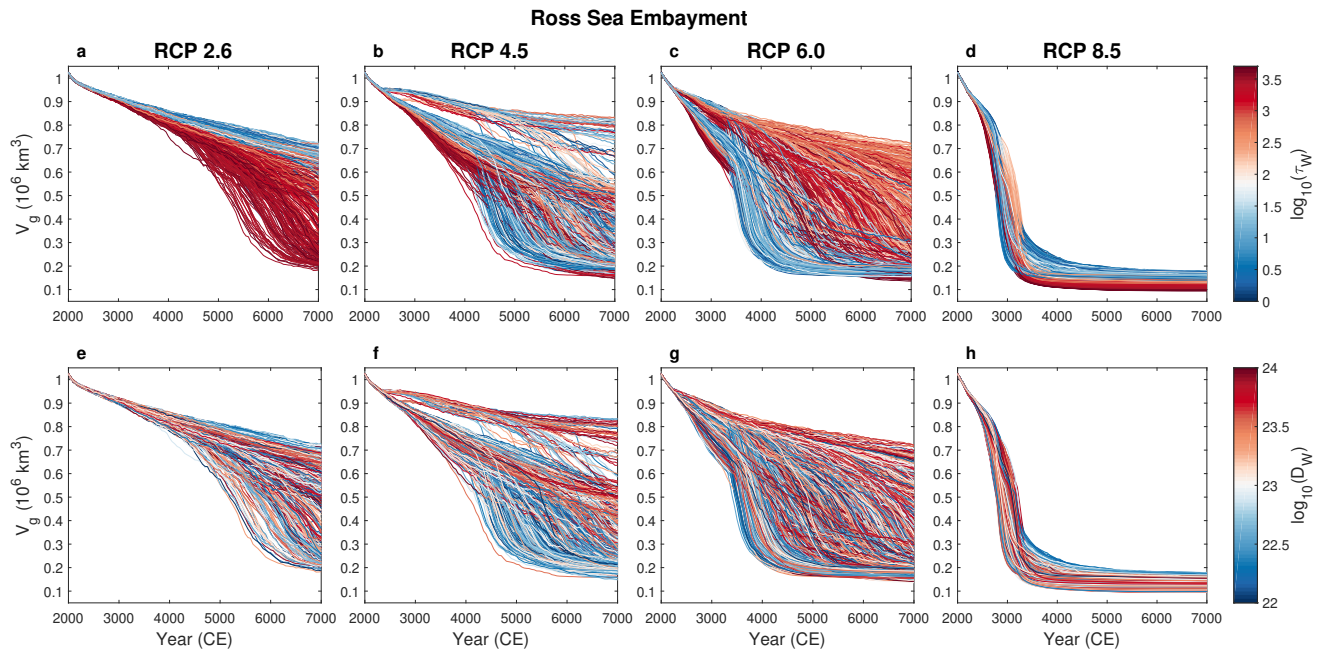


Figure S11. Evolution of Ross Sea Embayment grounded-ice volume (V_g) under RCP 2.6 (a, e), 4.5 (b, f), 6.0 (c, g), and 8.5 (d, h) for 2000 Monte Carlo samples from the parameter space. Time-series of the ensemble are color-coded by values of (a–d) $\log_{10}(\tau_w)$ and (e–h) $\log_{10}(D_w)$. Units for D_w are N m and units for τ_w are years.

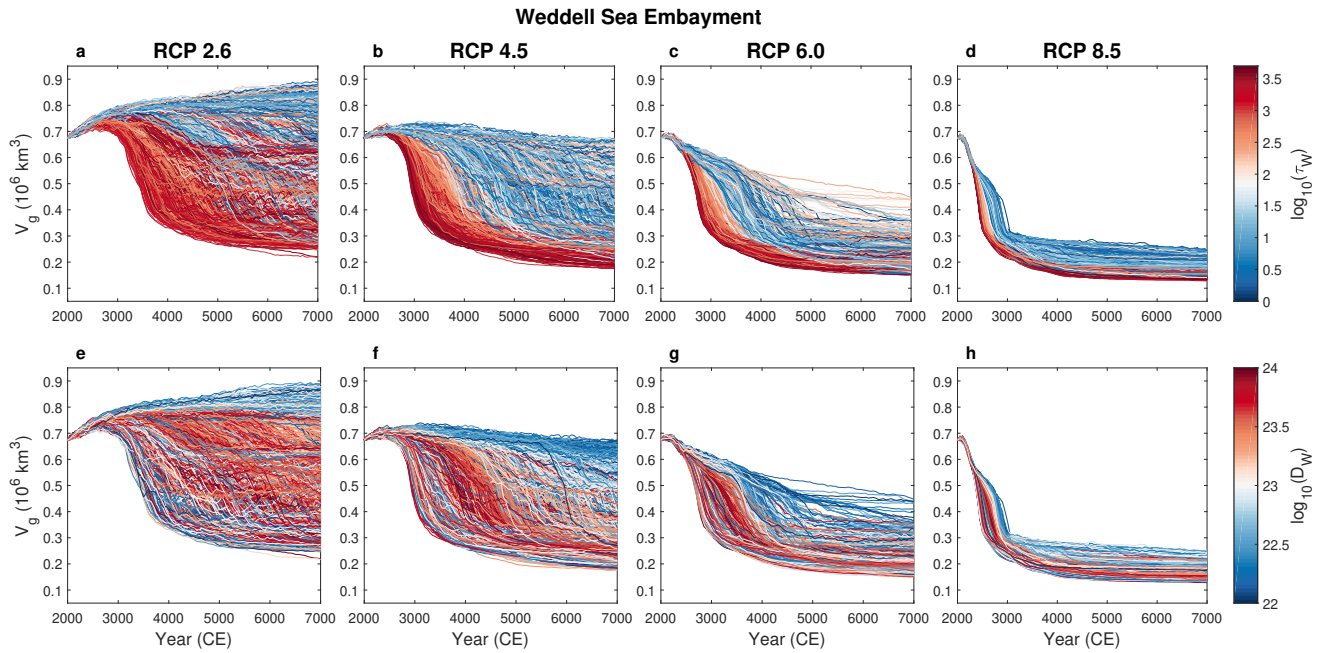


Figure S12. Evolution of Weddell Sea Embayment grounded-ice volume (V_g) under RCP 2.6 (a, e), 4.5 (b, f), 6.0 (c, g), and 8.5 (e, h) for 2000 Monte Carlo samples from the parameter space. Time-series of the ensemble are color-coded by values of (a–d) $\log_{10}(\tau_w)$ and (e–h) $\log_{10}(D_w)$. Units for D_w are N m and units for τ_w are years.

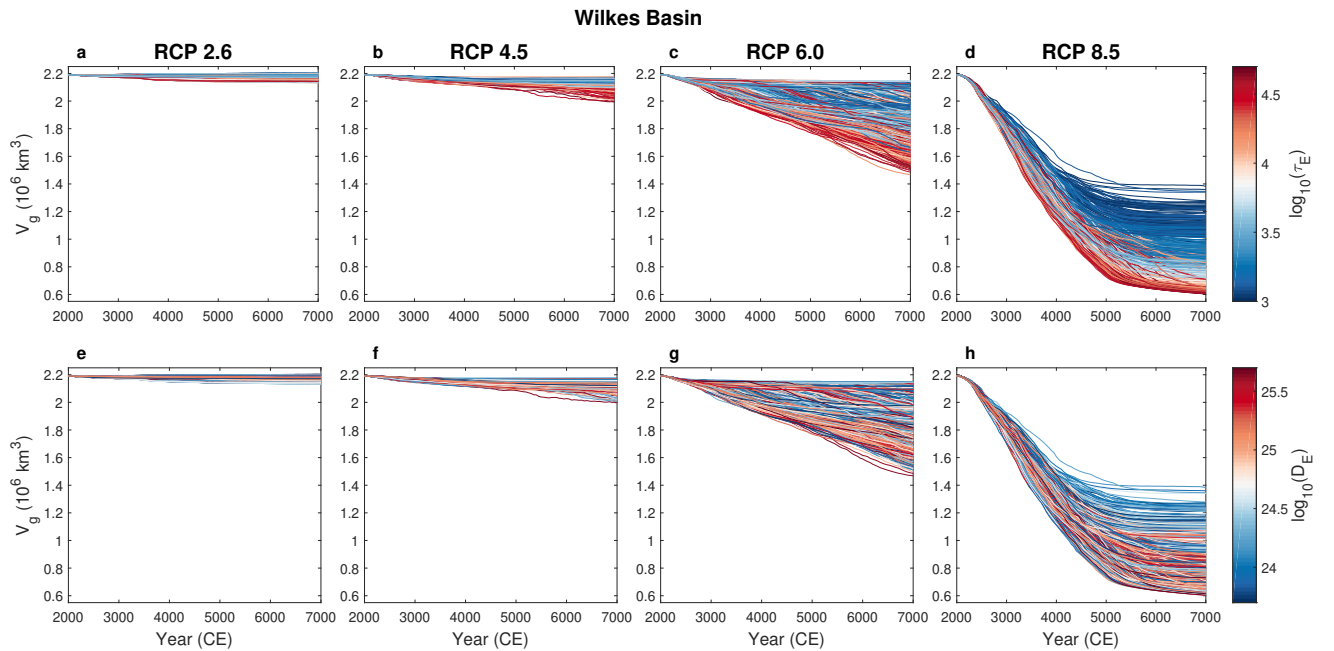


Figure S13. Evolution of Wilkes Basin grounded-ice volume (V_g) under RCP 2.6 (a, e), 4.5 (b, f), 6.0 (c, g), and 8.5 (d, h) for 2000 Monte Carlo samples from the parameter space. Time-series of the ensemble are color-coded by values of (a–d) $\log_{10}(\tau_E)$ and (e–h) $\log_{10}(D_E)$. Units for D_E are N m and units for τ_E are years.

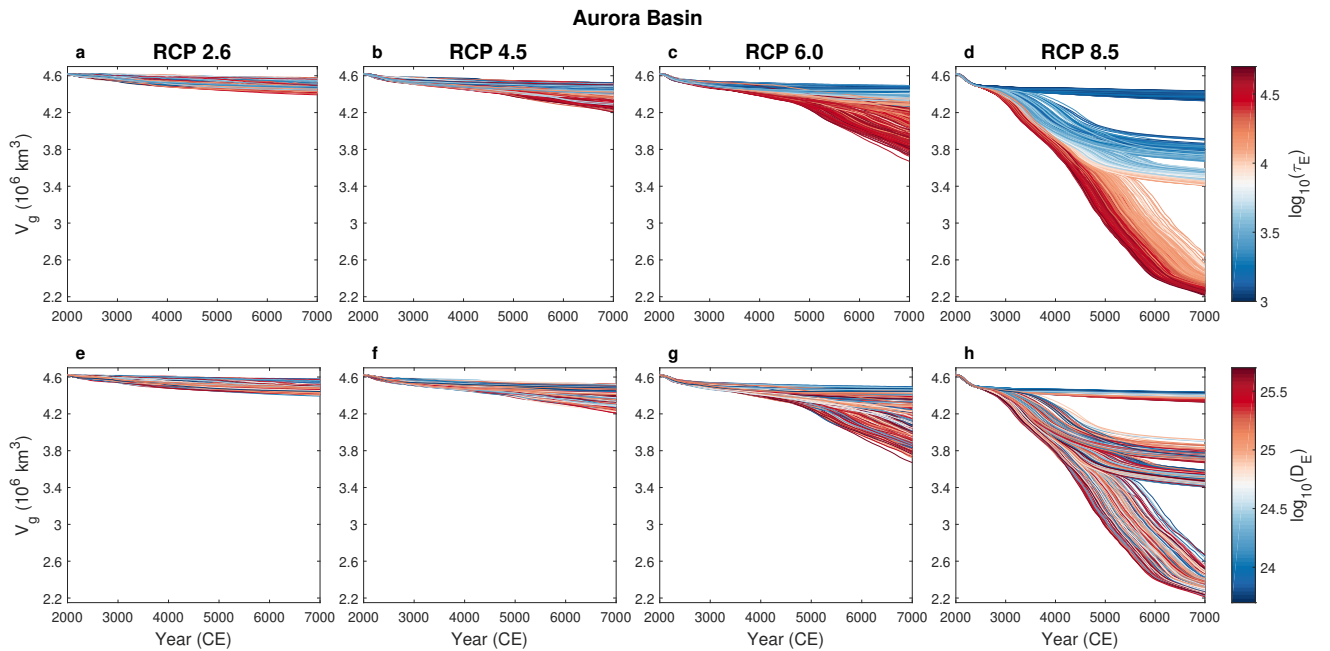


Figure S14. Evolution of Aurora Basin grounded-ice volume (V_g) under RCP 2.6 (a, e), 4.5 (b, f), 6.0 (c, g), and 8.5 (e, h) for 2000 Monte Carlo samples from the parameter space. Time-series of the ensemble are color-coded by values of (a–d) $\log_{10}(\tau_E)$ and (e–h) $\log_{10}(D_E)$. Units for D_E are N m and units for τ_E are years.

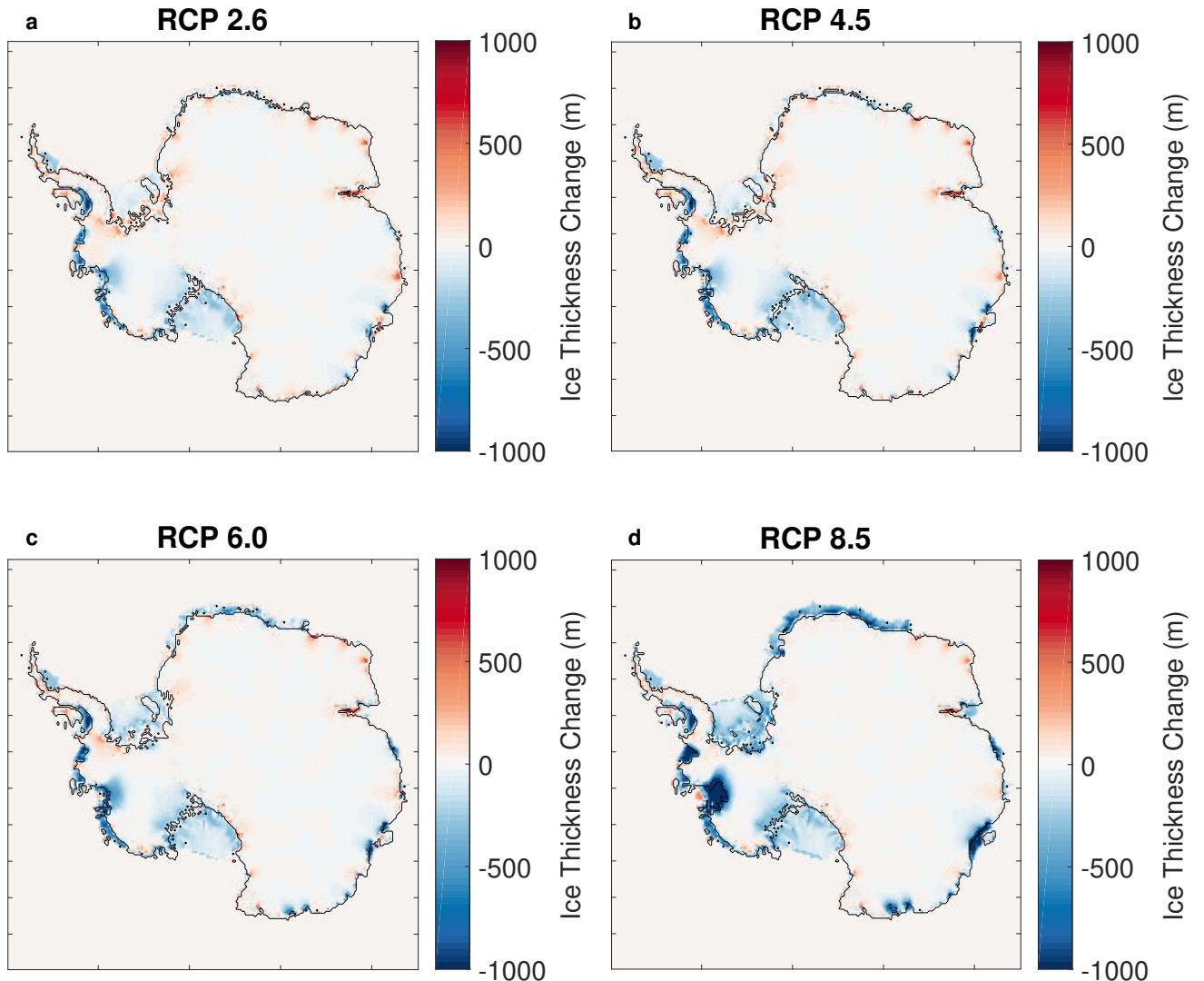


Figure S15. Ice thickness change at 2300 CE under RCP (a) 2.6, (b) 4.5, (c) 6.0, and (d) 8.5 for a simulation with uniform ELRA parameters (UNIBED) taken from Le Meur and Huybrechts (1996) and for which only bedrock adjustment is considered, i.e. gravitationally-consistent sea-level changes are not included.

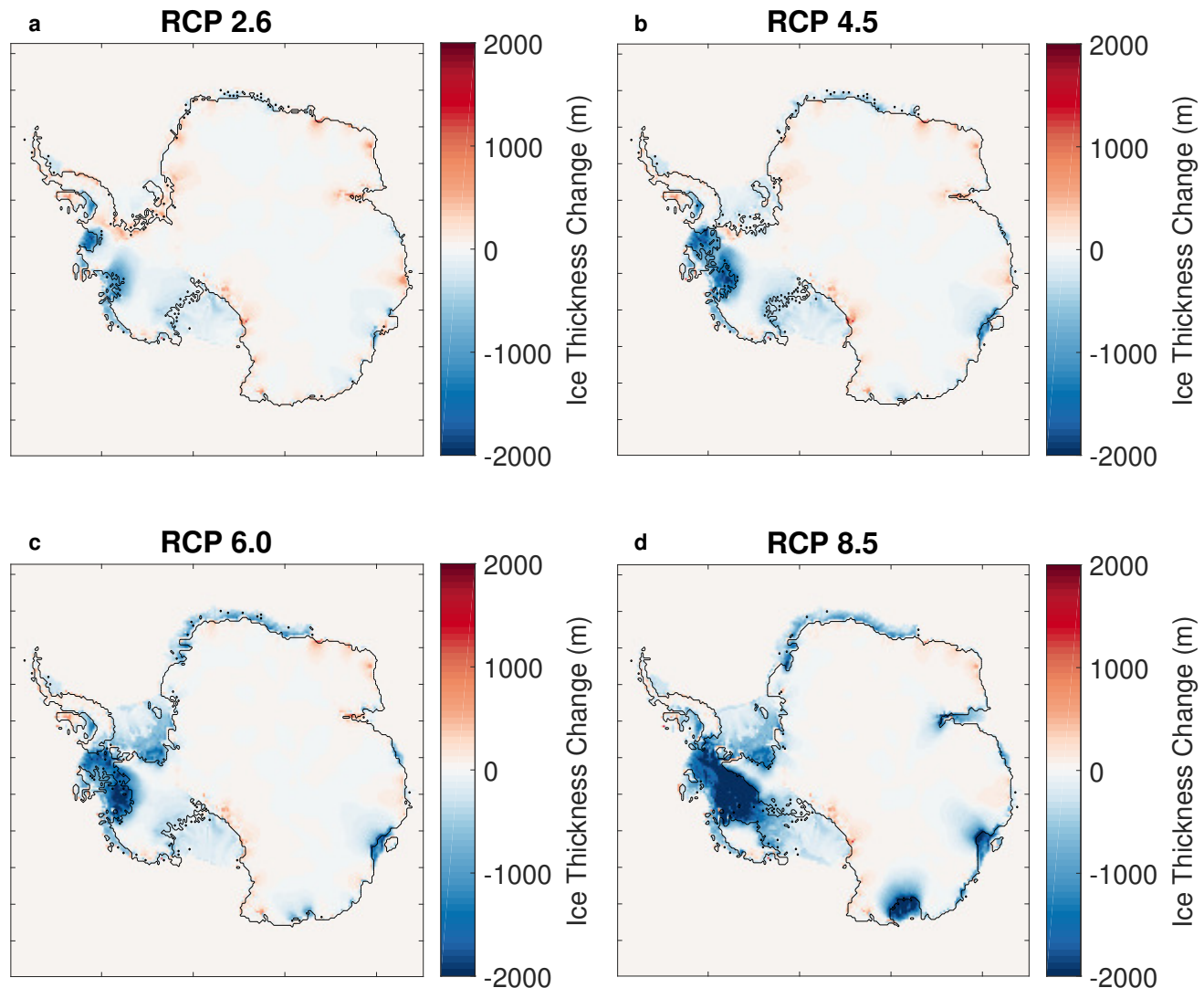


Figure S16. Ice thickness change at 3000 CE under RCP (a) 2.6, (b) 4.5, (c) 6.0, and (d) 8.5 for a simulation with uniform ELRA parameters (UNIBED) taken from Le Meur and Huybrechts (1996) and for which only bedrock adjustment is considered, i.e. gravitationally-consistent sea-level changes are not included.

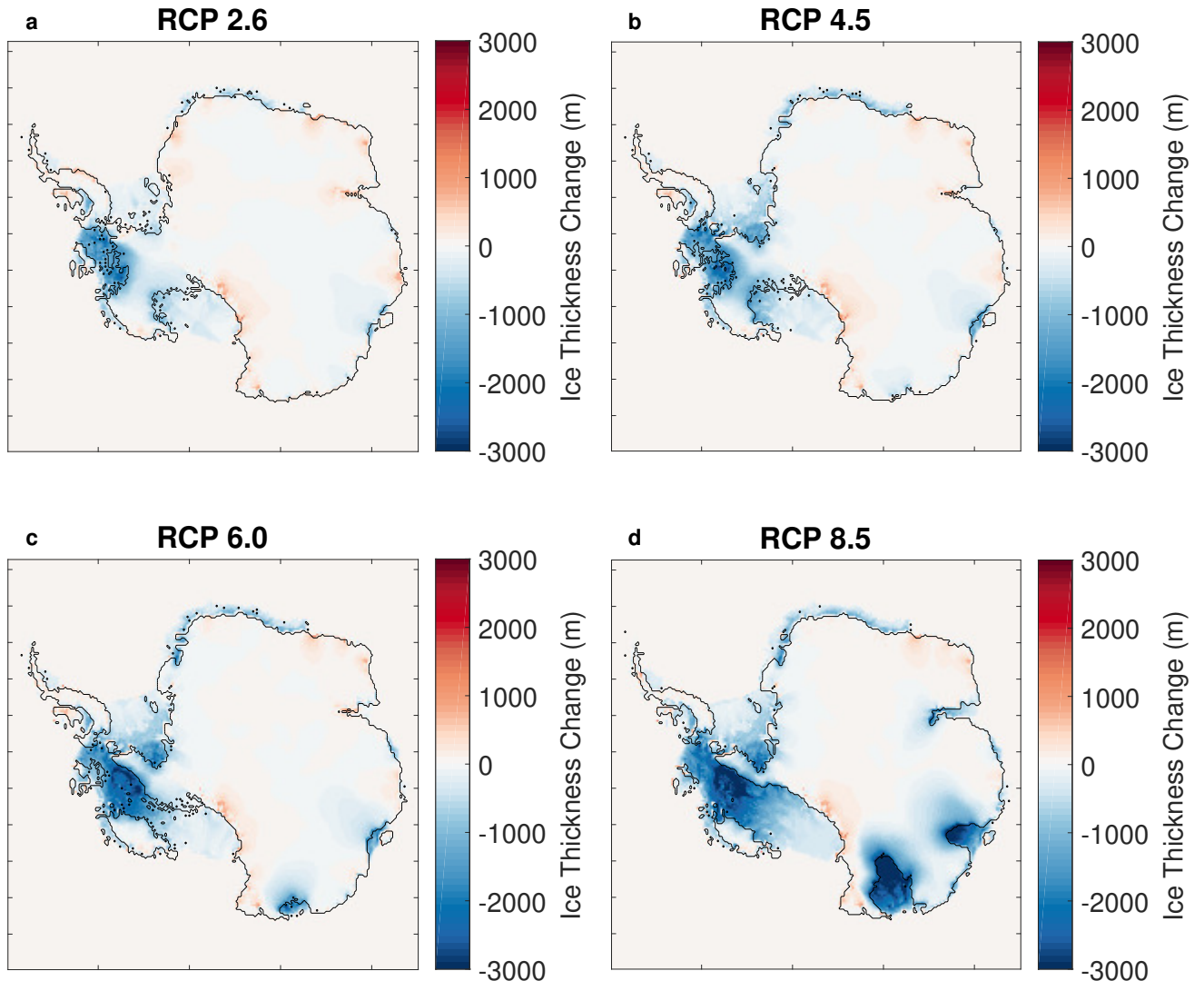


Figure S17. Ice thickness change at 5000 CE under RCP (a) 2.6, (b) 4.5, (c) 6.0, and (d) 8.5 for a simulation with uniform ELRA parameters (UNIBED) taken from Le Meur and Huybrechts (1996) and for which only bedrock adjustment is considered, i.e. gravitationally-consistent sea-level changes are not included.

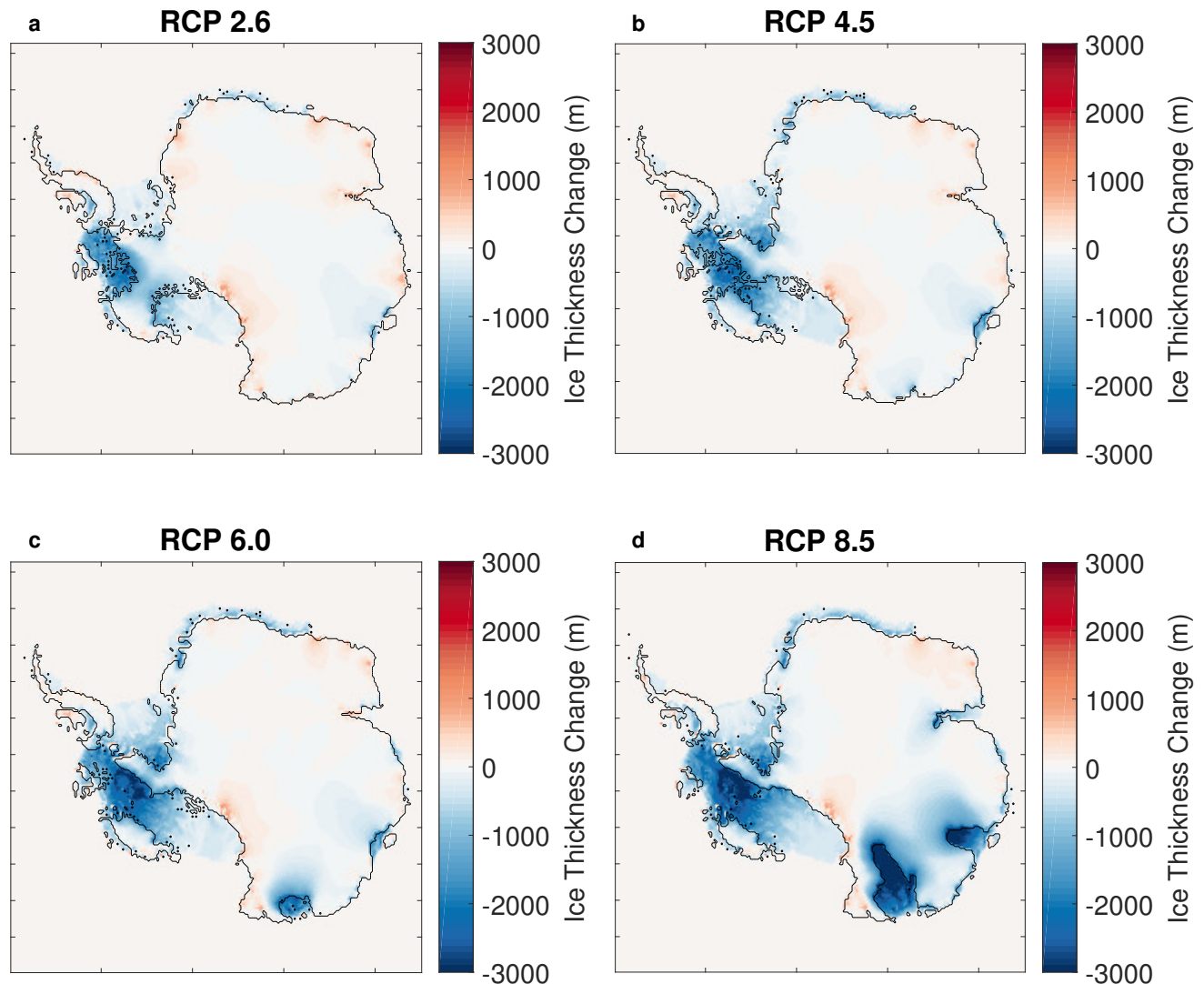


Figure S18. Ice thickness change at 7000 CE under RCP (a) 2.6, (b) 4.5, (c) 6.0, and (d) 8.5 for a simulation with uniform ELRA parameters (UNIBED) taken from Le Meur and Huybrechts (1996) and for which only bedrock adjustment is considered, i.e. gravitationally-consistent sea-level changes are not included.

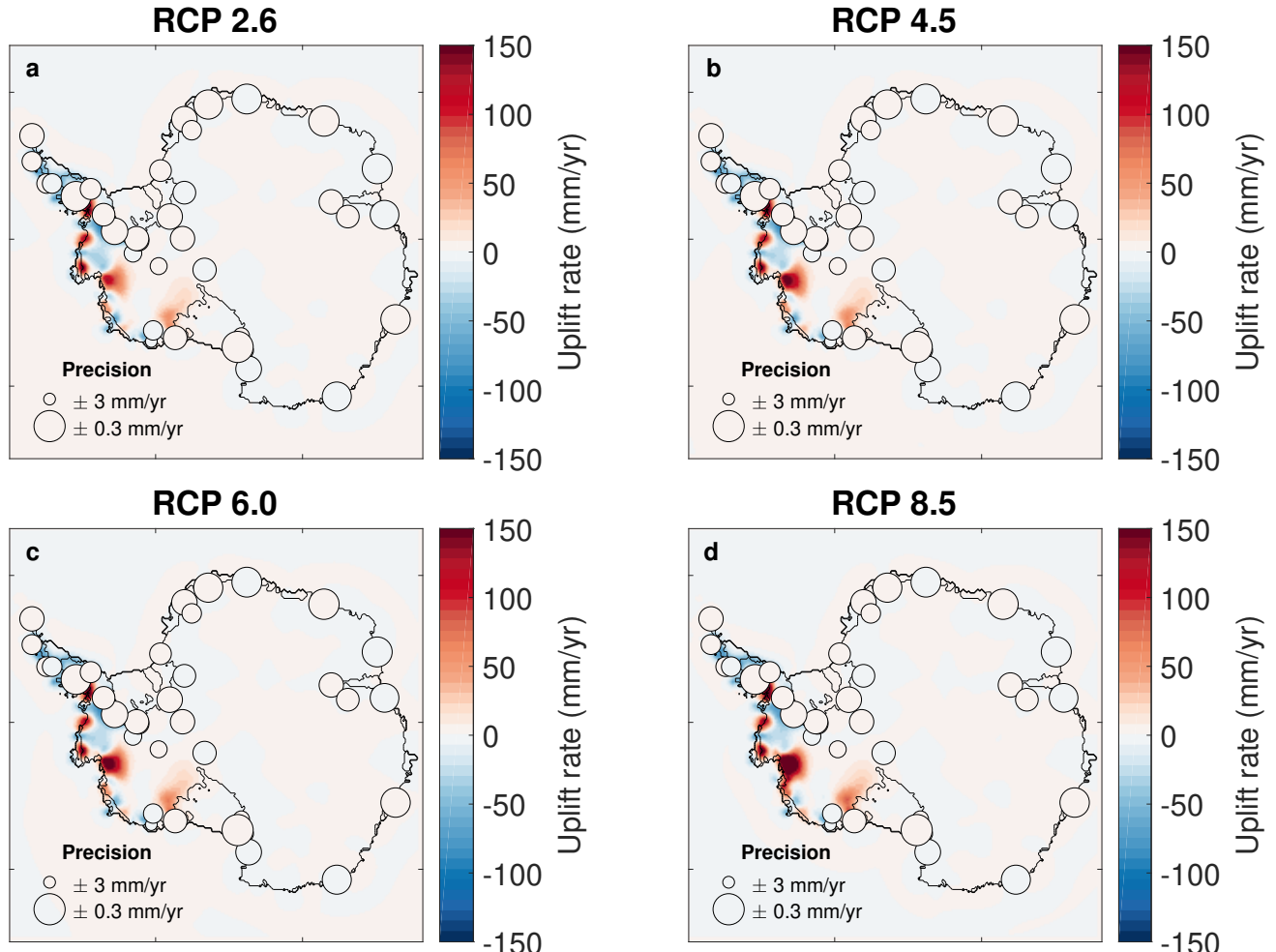


Figure S19. Mean uplift rates maps at 2100 CE predicted by the ensemble of 2000 Monte Carlo simulations under RCP (a) 2.6, (b) 4.5, (c) 6.0, and (d) 8.5. GPS observations of present-day uplift rates from Whitehouse, Bentley, Milne, et al. (2012) are plotted (colored circles) using the same colour scale. The radius of the circle at each GPS site is inversely proportional to the GPS uncertainty at that site.